Defects Characterization of HgCdTe and CdZnTe Compounds by Positron Annihilation Spectroscopy

Valentin Léger, Pierre Desgardin, Vincent Destefanis, Jacques Botsoa, Gilles Patriarche, Marie-France Barthe, Catherine Corbel, Laurent Rubaldo

DEFECTS CHARACTERIZATION OF HgCdTe AND CdZnTe COMPOUNDS BY POSITRON ANNIHILATION SPECTROSCOPY

Valentin Léger[(1)], Pierre Desgardin [(2)], Vincent Destefanis[(3)], Jacques Botsoa[(2)], Gilles Patriarche[(1)], Marie-France Barthe[(2)], Catherine Corbel [(4)], Laurent Rubaldo [(3)]

[(1)] C2N, 10 Boulevard Thomas Gobert, 91120 Palaiseau, France
[(2)] CEMHTI-UPR3079 CNRS, CS 30058, 3A rue de la Férolerie 45071, Orléans Cedex 2, France
[(3)] Lynred, 364 avenue de Valence, 38113 Veurey-Voroize, France
[(4)] LSI, CEA/DRF/IRAMIS, CNRS, Ecole polytechnique, Institut Polytechnique de Paris, 91120 Palaiseau, France
e-mail: valentin.leger@universite-paris-saclay.fr

ABSTRACT

IR cooled photodetectors need to operate at higher temperature to reduce their size, weight and power consumption (SWaP context). Their stability and image quality are then challenged by an extra electrical activity of crystal defects. Knowledge of defect populations is mandatory to improve the material quality of the epitaxial $Hg_{1-x}Cd_xTe$ (MCT) active layer and the $Cd_{1-x}Zn_xTe$ (CZT) substrate. Positron annihilation spectroscopy (PAS) with a slow positron beam was used to study near-surface open-volume defects profiles. Low and high momentum fractions (S,W) were used to characterize the Doppler broadening of the 511 keV electron-positron pair annihilation-line as a function of the positron implantation energy E. The results show that three regions can be identified beneath the surface of the as-grown non-optimized MCT layer. The quasi-linear relationship between the annihilation characteristics in the regions suggests that the defect populations mainly correspond to the same open-volume defect in different concentrations. The probed defect is supposed to be related to the mercury vacancy. This hypothesis is discussed in an original way with near-surface elemental profiles using scanning transmission electron spectroscopy combined to energy dispersive X-ray spectroscopy (STEM-EDX). Afterwards, this approach is extended to CZT substrates showing that surface and bulk properties of those elaborated by LYNRED tend to the state of the art. A common open-volume defect is probed, in concentration estimated by Hall effect around 10^{15} cm^{-3} and supposed to be related to the cadmium vacancy.

Key words: II-VI single crystals, Epitaxial MCT, Bulk CZT, Positron Annihilation Spectroscopy, Positron Trapping, Open-volume Defects

INTRODUCTION

The current trend in the area of cooled infrared (IR) is to develop photodetectors with more compact geometry, lighter weight and lower energy consumption (SWaP context) for portable applications. The strategy employed is to increase the operating temperature in order to reduce the size of the cooling machine. The goal for extended mid-wave (MW) technologies based on $Hg_{1-x}Cd_xTe$ (MCT) alloy is the 130-150 K range. However, at higher temperatures than the standard ones, the pixel response is affected by an extra electrical activity of crystal defects that limits detector performances and image quality. Ongoing material improvements are then a key challenge for high operating temperature (HOT) photodetectors and require atomic scale characterizations of defect populations in the epitaxial MCT active layer and $Cd_{1-x}Zn_xTe$ (CZT) single crystal substrates.

Among the different techniques used to investigate crystal defects, positron annihilation spectroscopy (PAS) stands out for the detection of open-volume defects (vacancy, void, etc.) [1,2]. Positrons (e^+) are antiparticles of electrons (e^-). Once thermalized in matter, positrons have a survival probability that depends on the electron density. They annihilate with electrons by emitting gamma photons that carry away the energy and momentum of the e^+– e^-annihilating pairs. The energy, momentum and lifetime distribution of the e^+–e^-annihilating pairs vary with the positron quantum states in the material and are used as fingerprints of those states. In crystalline semiconductors, positrons can annihilate from various quantum states: Bloch states *i.e.* delocalized in the crystal lattice, open volume defect states *i.e.* localized after capture in the local potential well associated to the lack of positive atom nuclei, surface and interface states etc. The two-gamma annihilation mode is the dominant one in semiconductors, where the e^+– e^- annihilating pairs emit a Doppler broadened annihilation-ray centered at 511 keV (e^+ or e^- rest mass energy). PAS has been widely applied to identify defects via their open-volume, charge (neutral or negative) in elemental, III-V and II-VI semiconductor bulk crystals or layers [1,3]. Nonetheless, there is still a gap to fill for today's high quality compounds.

In this work, a low energy positron beam accelerator is used to vary the positron implantation depth to determine the near-surface open-volume defect profiles in two types of II-VI materials by recording the two-gamma annihilation line, $511 \pm \Delta E$ keV, as a function of positron energy E. This work highlights the sensitivity of PAS to open-volume defects in MCT epitaxial layers and CZT single crystals substrates. From the surface to around 9 $(a.u.)$ in the as-grown MCT layers, three regions can be identified where the defect concentration remains quasi-homogeneous while varying with the layers. In the CZT single crystals, only one homogeneous region is detected beneath the surface. The positron annihilation characteristics in this region have close values

in the CZT single crystals although supplied from two different companies. The small variations of the annihilation characteristics most likely reflect the presence of supplier dependent low concentration of clean or residual impurity decorated Cd vacancy.

In addition to PAS, for one of extra MCT layer, near-surface elemental profiles are performed on cross sections using scanning transmission electron spectroscopy combined to energy dispersive X-ray spectroscopy (STEM-EDX). The correlation between PAS and STEM-EDX is discussed in an original way assuming that the depth profiling of the positron annihilation characteristics reflect the existence of a concentration gradient concentration for mercury vacancy beneath the surface.

EXPERIMENTAL DETAILS

II-VI MATERIALS

The epitaxial $Hg_{0.69}Cd_{0.31}Te$ layer [4,5] with 47 × 48 mm² area and thickness in the 5-10 µm range was grown by liquid-phase epitaxy (LPE) technique on (111) $Cd_{1-x}Zn_xTe$ substrate [5]. The epitaxy is not optimized, without chemical etching after growth and stored in air a few weeks before characterization. The as-grown layer is *p*-type conducting with hole concentration around several 10^{16} cm^{-3} at 80 K. From this MCT layer, two samples were cut with 10 × 10 mm² area: B2 and D4. The CZT single crystal substrates are from two different suppliers: an optimized LYNRED and a state of the art from another company. Both types were grown by vertical gradient freeze (VGF) technique, then mechanically polished, chemically etched and stored in air a few weeks before characterization. The crystals have close composition with low Zn fraction ($x \ll 0.2$) and are *p*-type conducting with hole concentration of about 10^{15} cm^{-3} at 300 K. Two samples of each substrate were cut with 10 × 10 mm² area: I1 and I2 (optimized LYNRED), and E1 and E2 (state of the art).

NEAR-SURFACE OPEN-VOLUME DEFECT PROFILING TECHNIQUE

Near-surface open-volume defect profiles were performed at room temperature using the slow positron beam [7] at CEMHTI (Orléans, France), with a beam diameter of 6 mm. The momentum distribution of the $e^+ - e^-$ annihilating pairs for positron energy varying by steps of about $E_{max}/50$ is determined by recording the Doppler spectrum of the 511 keV annihilation-line with a high resolution germanium detector. About 10^6 annihilation events are recorded to obtain the Doppler spectra with a good statistic. More precisely, for the $e^+ - e^-$ annihilating pairs, one extracts the distribution of the longitudinal momentum component p_L, parallel to the

emission direction of one of the two annihilation γ-ray ($E_\gamma = m_0c^2 \pm \Delta E$), from the measured Doppler broadening ($2\Delta E = p_L c$) [2]. The Doppler spectra are analyzed with two conventional line shape parameters S and W, which represent respectively the fractions of thermalized positrons annihilating with low and high momentum electrons. The low and high momentum fractions (S,W) are defined with the following energy windows $\left|E_\gamma(p_L) - 511\ keV(p_L = 0)\right| < 0.636\ keV$ ($2.49 \times 10^{-3} m_0c$) and $2.46\ keV$ ($9.63 \times 10^{-3} m_0c$) $< \left|E_\gamma(p_L) - 511\ keV(p_L = 0)\right| < 6.35\ keV$ ($24.85 \times 10^{-3} m_0c$). Experimental values for (S,W) in a material directly depend on the electrons available for annihilation from the different positron quantum states. For each quantum state, annihilations with valence electrons of low momentum contribute most to S whereas core electrons with higher momentum contribute most to W. The experimental profiles as a function of positron beam energy $S(E)$ and $W(E)$ are fitted with the VEPFIT [8] program to determine the annihilation probabilities $f(E)$ and characteristics (S,W) at surface and in the material divided in i homogeneous regions, equations (1). The positron transport is calculated from a time-independent one-dimensional equation describing the positron diffusion in the material and its return to the surface.

$$\begin{aligned} S(E) &= f_{Surf}(E).S_{Surf} + \sum_i f_i(E).S_i \\ W(E) &= f_{Surf}(E).W_{Surf} + \sum_i f_i(E).W_i \\ f_{Surf}(E) &+ \sum_i f_i(E) = 1 \end{aligned} \quad (1)$$

NEAR-SURFACE ELEMENTAL PROFILING TECHNIQUE

Near-surface elemental profiles were performed at nanoscale and room temperature using STEM-EDX at C2N (Palaiseau, France). A cross-section of a third sample (B1) cut from the MCT layer and not measured by PAS was prepared using a focused ion beam (FIB). The surface was coated with 50 nm of carbon to protect it from the platinum mask deposited for the milling process. TEM/STEM observations were made on a Titan Themis 200 microscope (FEI/ Thermo Fischer Scientific) equipped with a geometric aberration corrector on the probe. The microscope is also equipped with the "Super-X" systems for EDX analysis with a detection angle of 0.9 steradian. Observations are made at 200 kV with a probe current of about 70 pA and a half-angle of convergence of 17 mrad. High-angle annular dark-field (HAADF) images are acquired with a camera length of 110 mm (inner/outer collection angles are respectively 69 and 200 mrad).

RESULTS AND DISCUSSION

EPITAXIAL $Hg_{0.69}Cd_{0.31}Te$ LAYER

In Fig.1, one notices that the curves $S(E)$ and $W(E)$ exhibit distinctive features for both B2 and D4 MCT layers with increasing positron implantation energy E. One weak local extremum appears in $S(E)$ whereas $W(E)$ shows two local extrema. The variations between $S(E)$ and $W(E)$ are correlated as follows in the B2 layer. From the surface, $S(E)$ and $W(E)$ first increase when positrons get implanted deeper up to the energy $E_1(a.u.) \approx 0.9$. Then as energy increases further, $W(E)$ goes through a local maximum for the energy E_1 whereas $S(E)$ goes on increasing. One notices that, as the positron implantation energy reaches $E_2(a.u.) \approx 1.9$, a weak maximum in $S(E)$ corresponds to a local mimimum in $W(E)$. The correlation between $S(E)$ and $W(E)$ has similar features in the D4 layer with the energy values: $E_1(a.u.) \approx 1.3$ in and $E_2(a.u.) \approx 2.8$.

The type of correlation observed in Fig.1 between the variations of $S(E)$ and $W(E)$ suggests the existence of three regions beneath the surface, R_i (i = 1,2,3), with distinct annihilation characteristics (S_i, W_i). For positron implantation energy in the range of 0.08 to E_1, the probability of annihilation at surface with annihilation characteristics (S_{surf}, W_{surf}) decreases to the benefit of R_1 with the characteristics (S_1, W_1). For the range of E_1 to E_2, the probability of annihilation decreases in R_1 to the benefit of R_2 with annihilation characteristics (S_2, W_2). For the range E_2 to E_{max}, the probability of annihilation decreases in R_2 to the benefit of R_3 with annihilation characteristics (S_3, W_3). It follows from the $S(E)$ and $W(E)$ variations that the annihilation characteristics verify the relationships (2).

$$(S_{surf} < S_1, W_{surf} < W_1);\ (S_1 < S_2, W_1 > W_2);\ (S_2 > S_3, W_2 < W_3) \quad (2)$$

The comparison of those relationships indicates that the chemical environment where positrons annihilate differs between the surface and the first region R_1. Furthermore, the region R_2 is the region where (S, W) reaches their extreme values, a higher and a lower one for S_2 and W_2 respectively.

The positron implantation energy dependences of the low and high momentum $S(E)$ and $W(E)$ are calculated and consistently fitted to the experimental curves in Fig. 1 using the fitting program VEPFIT. The fitting of the experimental data $S(E)$ and $W(E)$ requires to define at least three regions beneath the surface. Positron implantation, transport, annihilation probability and characteristics are calculated as a function of positron energy at each iteration step with the following quantities as parameters: the region thickness Δz_i which is finite for $R1$, $R2$ and infinite for R_3, the mass density ρ_i, the effective positron diffusion length, $L^+_{i,eff}$ and

annihilation characteristics in each region (S_i, W_i) and the surface (S_{surf}, W_{surf}). In this work, the positron implantation profile in VEPFIT is calculated in each region for mass density equal to the value ρ = 7.385 g.cm^{-3} for $Hg_{0.69}Cd_{0.31}Te$ [9]. To reduce the number of free parameters, the fit has been tested by fixing various region thicknesses. The modeling requires thicknesses higher for the D4 layer than the B2 layer: $R1_{B2}(a.u.) = 2$, $R1_{D4}(a.u.) = 5$, $R2_{B2}(a.u.) = 2$ and $R2_{D4}(a.u.) = 4$ (Fig. 2). This is mandatory to reproduce the $W(E)$ extrema at higher energies for D4 than B2.

In Fig. 3, one can notices an interesting property in the $S(W)$ graph where the fitted values of the annihilation characteristics (S_{surf}, W_{surf}) and (S_i, W_i) are plotted for both layers B2 and D4. The fitted values for each region R_i (i = 1,2,3) fall on a same straight line (red dotted line) for both layers. Such straight lines are obtained when two distinct annihilation quantum states with specific annihilation fingerprints are superimposed [10-12]. Between the two quantum states, only the positron annihilation probability varies. Here, the straight line in Fig. 3 has a negative slope $dS/dW < 0$. Such slopes are associated with positron annihilation probability varying between two quantum states with annihilation fingerprints arising from different open–volumes [13]. The fingerprints for annihilation from the smaller (S_o, W_o) and bigger open-volume (S_O, W_O) verify the relationships (3).

$$\left(S_o < S_1(B2), W_o > W_1(B2);\ S_O < S_2(D4), W_O > W_2(D4)\right) \tag{3}$$

In the high purity B2 and D4 MCT LPE layers, the p-type conductivity is usually controlled by the double acceptors that are mercury monovacancies. This leads to the simple identification of the annihilation fingerprints (S_o, W_o) to the delocalized state in lattice and (S_O, W_O) to the localized state in V_{Hg}^{2-}. This identification is consistent with previous positron lifetime [14-16] and Doppler broadening [17-19] experiments which all highlight the positron trapping by the mercury vacancy when those control p-type doping. The regions R_i (i = 1,2,3) reflect the existence of a gradient of positron capture in the Hg vacancy beneath the surface induced by a depth gradient of the Hg vacancy concentration.

An interesting feature is that the V_{Hg} concentration for the deeper region R_3 clearly appears to be the closer in both layers. The annihilation characteristics (S_3, W_3) in the B2 and D4 layers differ respectively by at most (0.2 %, 0.6 %). Another feature worth to be noticed is the difference in the extension of the regions R_1 and R_2, *i.e.* the perturbed regions in reference to R_3. The first two regions extend over depth much larger in the D4 layer, about 10 $(a.u.)$, than in the B2 layer, about 4 $(a.u.)$. This suggests that there is heterogeneity in the

process resulting into the formation of the regions R_1 and R_2, and in the modulation of the V_{Hg} concentration. An intriguing feature is that the V_{Hg} concentration for the middle region $R2$ is the higher in both layers. The depth for this region is 3 $(a.u.)$ deeper in D4 than in B2.

In Fig. 4, the normalized elemental fractions determined from STEM-EDX show the composition of the B1 layer from the surface to the bulk. One immediately notices that the profile is depleted in Hg and enriched in Cd and Te near the surface, while the profile with the nominal alloy composition becomes stable above 11 $(a.u.)$, *i.e.* in bulk. Three regions can be defined in Fig.4 by the variations of the normalized elemental fractions. The first region R_1 begins from the surface to around 6 $(a.u.)$, where the Cd fraction returns to the bulk value unlike Hg and Te fractions. The second region R_2 extends up to 11 $(a.u.)$ where Hg and Te fractions return to the bulk values. The third region R_3 for depths greater than 11 $(a.u.)$ corresponds to a region where elemental fractions fluctuate while remaining in average stable and equal to the nominal composition $Hg_{0.70}Cd_{0.30}Te$.

The B1 layer was cut in an area representative of the D4 layer. An interesting point is that the number of region identifiable in STEM-EDX profiles is the same as for PAS profiles, with thicknesses close to those of the D4 layer: 6 $(a.u.)$ for R1 and 5 $(a.u.)$ for $R2$. In addition, due to the non-stoichiometry highlighted beneath the surface (Fig. 4), the correlation between a STEM-EDX region depleted in Hg and a PAS region with higher Hg vacancy concentration is possible. Therefore, elemental gradients observed by STEM-EDX are in good agreement with Hg vacancy concentration gradients obtained by PAS analysis for the as-grown non-optimized epitaxy.

$Cd_{1-x}Zn_xTe$ SINGLE CRYSTAL SUBSTRATES

Low and high momentum fractions (S,W) as a function of the positron implantation energy E in CZT substrates have similar features for both optimized LYNRED ones (I1 and I2) and othen supplier state of the art ones (E1 and E2). These profiles are illustrated for I2 in Fig. 5. One notices that S and W vary in opposite way with increasing positron energy from extrema at surface towards saturation into bulk. To fit these curves with VEPFIT, a model with one unique homogeneous region is sufficient (Fig.6). The fitted values for surface and the region with the $Cd_{1-x}Zn_xTe$ density (ρ = 5.85 g.cm^{-3}) [20] are reported in Fig.7 for the four crystal samples. The annihilation characteristics (S,W) for all samples are close and differ respectively at most by (0.3 %, 2.3 %) at surface and (0.08 %, 1.3 %) inside the region. This noticeable feature shows that, at 300 K, there is a good

reproducibility and equivalent crystal quality between the state of the art and the optimized LYNRED ones by positron annihilation characterization.

A recent paper [21] shows that the positron annihilation lifetime spectra vary strongly with the composition of $Cd_{1-x}Zn_xTe$ alloys, depending whether Cd rich or Zn rich compounds. In the present case, the alloy composition is Cd rich ($x << 0.2$). According to this study, the lifetime spectra become quite close to those in CdTe as the Cd fraction increases in the alloy. Hall measurements at 300 K shows that the crystals are intrinsically p-type doped with hole concentration around 10^{15} cm^{-3}. If assumed that this doping is only due to Cd vacancy, as commonly accepted [22], positrons are mainly trapped by these open-volume defects in low concentration. Cadmium vacancy concentrations are then rather reproducible in the four samples.

Literature shows that depending on the crystal history (conduction-type, doping level, growth technique, etc.) positron annihilation characteristics can vary in CdTe and CZT crystals due to the presence of defects with different natures and concentrations. Observed defects can vary from monovacancies [21,23-25], divacancies [11,21,25,26], vacancy-impurity complex [26,27], dopant-vacancy complexes (A-centers) [1]. Crystals with no positron traps have also been observed [28,29]. More work is in progress to examine whether a correlation can be established between the hole concentration and the positron annihilation features in CZT crystals nominally undoped.

CONCLUSION

In summary, the very high sensitivity of the positron as an atomic probe allowed to characterize the open-volume defects present in several II-VI compounds. Indeed, Doppler broadening profiles in as-grown non-optimized $Hg_{0.69}Cd_{0.31}Te$ LPE showed that three different regions can be identified beneath the surface. Each region differs with the concentration of a same open-volume defect which is probably related to the Hg vacancy. By careful analysis this PAS technique allowed us to make qualitative profiles of Hg vacancy in the near surface region. This result has been correlated in an original way with STEM-EDX elemental profiles, where three regions have also been identified with similar thicknesses. The non-stoichiometry of the two first regions supports the V_{Hg} gradients observed by PAS. In addition, PAS have shown that $Cd_{1-x}Zn_xTe$ substrates elaborated by LYNRED tend toward similar surface and bulk annihilation properties at 300 K than for state of the art substrates. The annihilation in the substrates most likely arises from a common open-volume defect which is probably related to the Cd vacancy in low concentration estimated from Hall measurements to be around 10^{15} cm^{-3}). This work will be deepened with temperature dependent Doppler broadening profiles and positron-

lifetime spectra associated with complementary characterizations such as cathodoluminescence at low temperature.

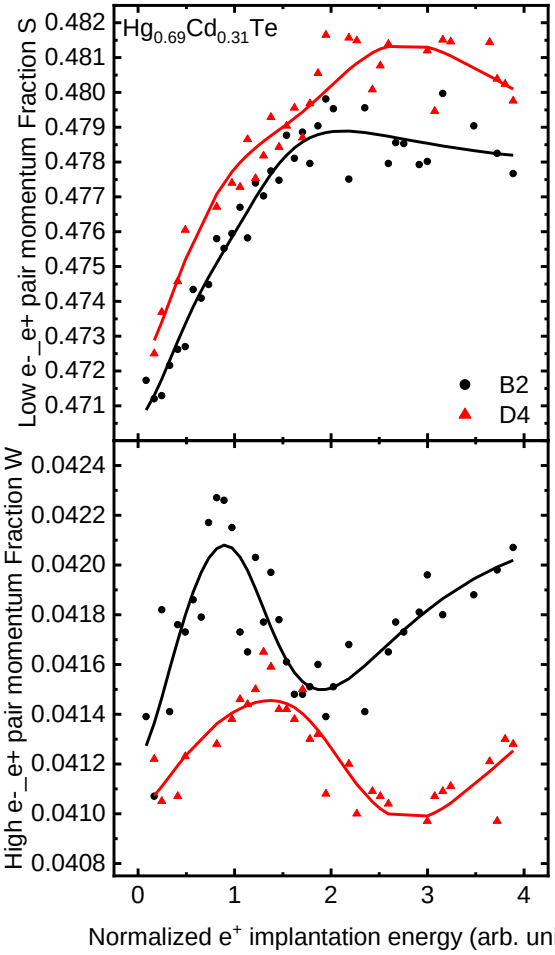

Fig. 1. Low momentum fraction S and high momentum fraction W as a function of the positron implantation energy E for the non-optimized as-grown $Hg_{0.69}Cd_{0.31}Te$ epitaxy: B2 layer (circles) and D4 layer (triangles). Solid lines show VEPFIT fitted profiles in a model with three homogeneous regions and the surface.

Slow positrons →

Surface	Region 1 (R1)	Region 2 (R2)	Region 3 (R3)
S_{surf}	S_1	S_2	S_3
W_{surf}	W_1	W_2	W_3
	$L^+_{1,eff}$	$L^+_{2,eff}$	$L^+_{3,eff}$
2D	$\rho_1 = 7{,}385\ \mathrm{g.cm^{-3}}$	$\rho_2 = 7{,}385\ \mathrm{g.cm^{-3}}$	$\rho_3 = 7{,}385\ \mathrm{g.cm^{-3}}$
	$\Delta z_{1,B2} = 2\ a.u.$	$\Delta z_{2,B2} = 2\ a.u.$	$\Delta z_3 = \infty$
	$\Delta z_{1,D4} = 5\ a.u.$	$\Delta z_{2,D4} = 4\ a.u.$	

Fig. 2. VEPFIT model and parameters for the fitting of $S(E)$ and $W(E)$ profiles for the non-optimized as-grown $Hg_{0.69}Cd_{0.31}Te$ LPE layers. Each region i is described with the following set of parameters, fixed ones for the thickness Δz_i and the density ρ_i, and free ones for the effective positron diffusion length $L_{i,eff}^{+}$, and the low and high momentum fractions (S_i,W_i).

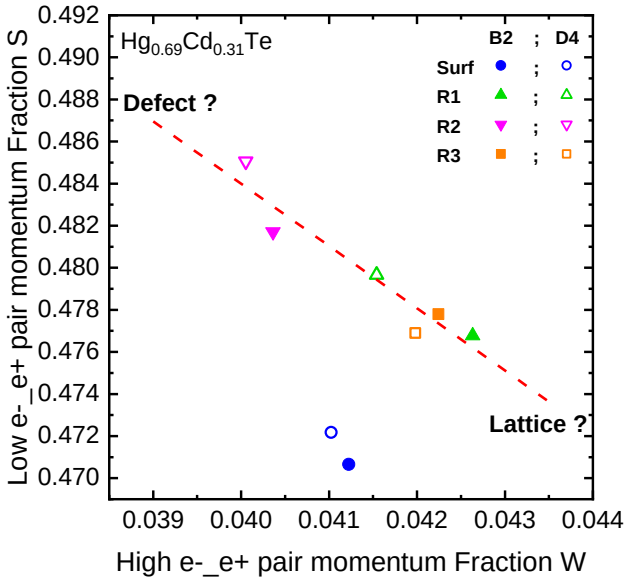

Fig. 3. Fitted values of the low momentum fraction S as a function of the high momentum fraction W for the non-optimized as-grown $Hg_{0.69}Cd_{0.31}Te$ LPE of B2 layer (filled symbols) and D4 layer (open symbols): surface (blue circles), first region (green triangles), second region (pink inverted triangles) and third region (orange squares).

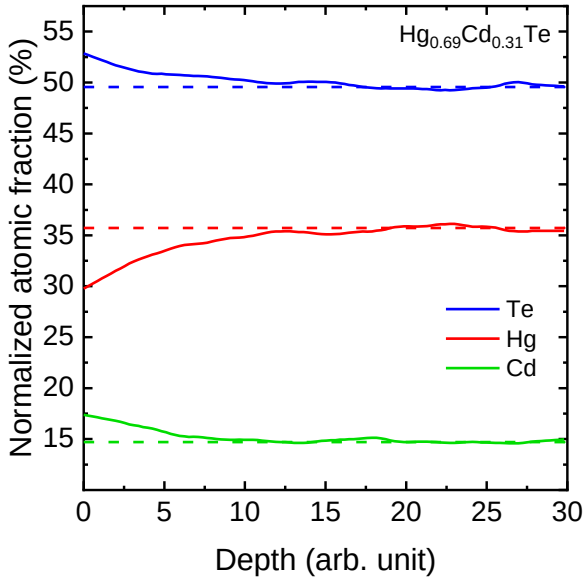

Fig. 4. Elemental profiles from the surface to the bulk of the non-optimized as-grown $Hg_{0.69}Cd_{0.31}Te$ LPE: telluride (blue line), mercury (red line) and cadmium (green line). Dotted lines represent mean bulk values of the nominal composition between 20 and 30 $a.u.$

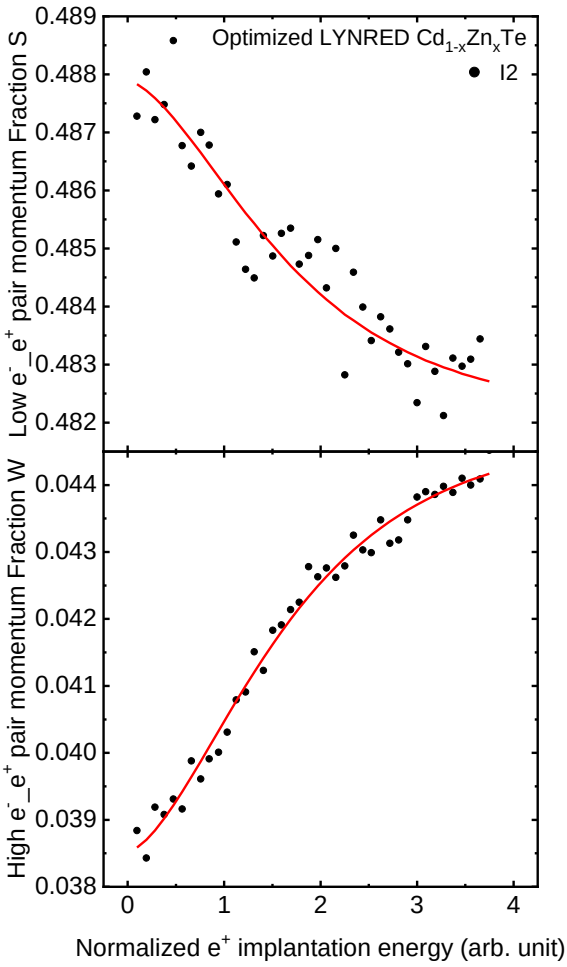

Fig. 5. Low momentum fraction S and high momentum fraction W as a function of the positron implantation energy E for the optimized LYNRED $Cd_{1-x}Zn_xTe$ substrate I2 (black symbols). Solid lines show VEPFIT fitted profiles in a model with a single homogeneous region and the surface.

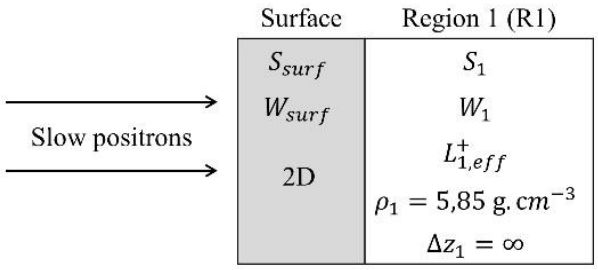

Fig. 6. VEPFIT model and parameters for the fitting of $S(E)$ and $W(E)$ profiles for the CZT substrates. The single region i is described with the following set of parameters, fixed ones for the thickness Δz_i and the density ρ_i, and free ones for the effective positron diffusion length $L^{+}_{i,eff}$, and the low and high momentum fractions (S_i,W_i).

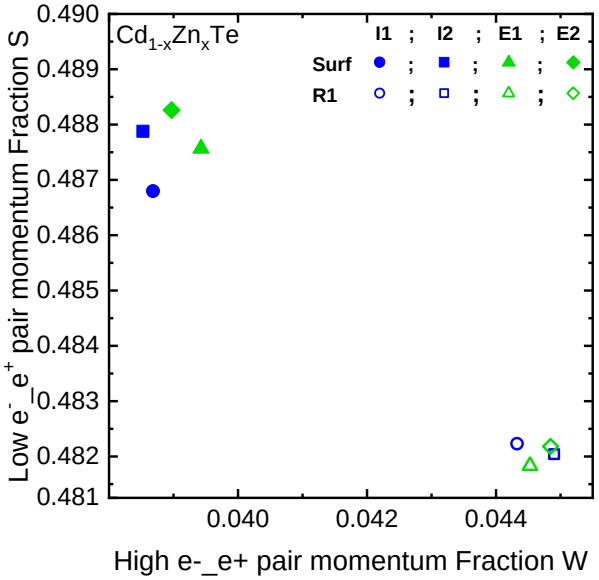

Fig. 7. Fitted values of the low momentum fraction S as a function of the high momentum fraction W at the surface (filled symbols) and inside the region (open symbols) for the $Cd_{1-x}Zn_xTe$ substrates: I1 (blue circles) and I2 (blue squares) from the optimized LYNRED CZT, and E1 (green triangles) and E2 (green diamonds) are state of the art from the other supplier.

REFERENCES

1. R. Krause-Rehberg, H.S. Leipner, Positron annihilation in semiconductors: Defect studies, 1st edn. (Springer-Verlag, Berlin Heidelberg, 1999)
2. P. Hautojärvi, Positrons in solids, 1st edn. (Springer-Verlag, Berlin Heidelberg, 1979)
3. F. Tuomisto and I. Makkonen, *Rev. Mod. Phys.* 85, 4 (2013)
4. B. Pelliciari, *Prog. Cryst. Growth Charact. Mater* 29, 1 (1994)
5. B. Pelliciari, J.P. Chamonal, G.L. Destefanis and L. Dicioccio, *Focal Plane Arrays: Technology and Applications*, Proc. SPIE 0865 (1988)
6. D. Brellier, E. Gout, G. Gaude, D. Pelenc, P. Ballet, T. Miguet and M.C. Manzato, *J. Electron. Mater.* 43, 2901 (2014)
7. P. Desgardin, L. Liszkay, M.F. Barthe, L. Henry, J. Briaud, M. Saillard, L. Lepolotec, C. Corbel, G. Blondiaux, A. Colder, P. Marie and M. Levalois, *Mater. Sci. Forum* 363-365 (2001)
8. A. van Veen, H. Schut, J. de Vries, R.A. Hakvoort and M.R. Ijpma, in *AIP Conference Proceedings* 218 (1991), p. 171
9. P. Capper, Properties of narrow gap cadmium-based compounds, 1st edn. (INSPEC, 1994)
10. S. Mantl and W. Triftshäuser, *Phys. Rev. B* 17, 4 (1978)
11. L. Liszkay, C. Corbel, L. Baroux, P. Hautojärvi, M. Bayhan, A.W. Brinkman and S. Tatarenko, *Appl. Phys. Lett.* 64, 11 (1994)
12. L. Liszkay, C. Corbel, L. Baroux, P. Hautojärvi, A. Declemy and P.O. Renault, *J. Phys. Condens. Matter* 7, 45 (1995)
13. M. Hakala, M.J. Puska and R.M. Nieminen, *Phys. Rev. B* 57, 13 (1998)
14. C. Gely, C. Corbel and R. Triboulet, *J. Phys. Condens. Matter* 2, 21 (1990)
15. R. Krause, A. Klimakow, F.M. Kiessling, A. Polity, P. Gille and M. Schenk, *J. Cryst. Growth* 101, 1 (1990)
16. L. Baroux, C. Corbel, F.M. Kiessling, S. Rolland, R. Granger, W. Hoerstel and R. Triboulet, *Phys. Rev. Lett.* 75, 3 (1995)
17. C. Smith, P.C. Rice-Evans, N. Shaw and D.L. Smith, *J. Phys. Condens. Matter* 4, 26 (1992)
18. C. Smith, P. Rice-Evans, N. Shaw and D.L. Smith, *Phil. Mag. Lett.* 67, 3 (1993)
19. C.D. Smith, P. Rice-Evans and N. Shaw, *Phys. Rev. Lett.* 72, 7 (1994)
20. P. Capper and J. Garland, Mercury cadmium telluride: Growth, properties and applications, 1st edn. (Wiley, 2010)

21. M. Gorgol, R. Zaleski, A. Kierys, D. Kamiński, K. Strzałkowski and K. Fedus, *Acta Cryst. B* 77, 4 (2021)

22. M.A. Berding, *Phys. Rev. B* 60, 12 (1999)

23. B. Geffroy, C. Corbel and M. Stucky, *Mater. Sci. Forum* 10-12, (1986)

24. C. Corbel, L. Baroux, F.M. Kiessling, C. Gély-sykes and R. Triboulet, *Mater. Sci. Eng. B* 16, 1 (1993)

25. D.J. Keeble, J.D. Major, L. Ravelli, W. Egger and K. Durose, *Phys. Rev. B* 84, 17 (2011)

26. G. Tessaro and P. Mascher, *J. Cryst. Growth* 197, 3 (1999)

27. M. Martyniuk and P. Mascher, *Physica B Condens. Matter.* 308-310, (2001)

28. L. Šedivý, J. Čížek, E. Belas, R. Grill and O. Melikhova, *Sci. Rep.* 6, 1 (2016)

29. H. Kauppinen, L. Baroux, K. Saarinen, C. Corbel and P. Hautojärvi, *J. Phys.: Condens. Matter* 9, 25 (1997)